Insights into Kelvin probe force microscopy data of insulator-supported molecules

Julia L. Neff
Institut für Physikalische Chemie, Johannes Gutenberg Universität Mainz, Duesbergweg 10-14, 55099 Mainz, Germany

Philipp Rahe*
Department of Physics and Astronomy, The University of Utah, 115 South 1400 East, Salt Lake City, Utah 84112-0830, USA
(Received 1 September 2014; revised manuscript received 28 January 2015; published 24 February 2015)

We present a detailed analysis and understanding of Kelvin probe force microscopy (KPFM) data for a system of point charges in a vacuum-dielectric tip-sample system. Explicit formulae describing the KPFM signal ΔV are derived for the two KPFM operation modes, namely amplitude modulation and frequency modulation (FM). The formulae allow for a physical interpretation of the resulting KPFM signal, reveal contributing parameters, and especially disclose an additive behavior. We numerically evaluate these equations and show exemplary KPFM slice data for a single point charge. The theoretical analysis is complemented by two-dimensional FM-KPFM maps obtained experimentally on 2,5-dihydrobenzoic acid on calcite (10.4). The molecules assemble in two coexisting phases understood as protonated and deprotonated molecules. The two-dimensional maps reveal a convex shape of the KPFM signal ΔV across the islands and a clear difference between the two phases is revealed. Furthermore, we apply the theoretically suggested difference strategy to extract the molecular component from the measured total KPFM signal.

DOI: 10.1103/PhysRevB.91.085424 PACS number(s): 68.37.Ps, 73.30.+y, 73.61.Ng, 77.55.−g

I. INTRODUCTION

The successful combination of atomic force microscopy [1] with the Kelvin probe technique [2], featuring the so-called Kelvin probe force microscopy [3], allows first and foremost mapping of work function differences on conducting and semiconducting samples. Over the past decades, Kelvin probe force microscopy (KPFM) became an indispensable tool for studying electronic properties at the meso- and microscales [4–6].

The systems investigated to the day span an impressive range from application-oriented photovoltaic materials [7–9] to metallic nanocontacts [10–12] and organic thin films [13–19] as well as individual adatoms [20,21] on metals, semiconductors, or insulators. Very recently, even submolecular contrast has been reported [19,22–24] and the KPFM technique has successfully identified the charge state of adsorbates [20,25,26].

On dielectric samples, KPFM has been employed to study step edges [27,28], point defects [29], and surface ions [21,30], to name but a few. Significant contrast differences have been revealed between the insulating support and adsorbates such as metallic nanoclusters [10,11], single charged adatoms [31], and organic molecules [16–18,32–36].

However, despite the large body of experimental and theoretical work [31,37–41] available nowadays, the detailed interpretation of the KPFM signal ΔV and its relation to the concept of the local work function [42] is especially for insulating substrates still a challenge. Furthermore, questions have been raised concerning the comparability of KPFM data obtained by the different KPFM measurement modes [17,43,44].

Here, we derive explicit formulae describing the KPFM signal ΔV for a system of point charges in a finite tip-sample capacitor containing dielectric material as the sample. This derivation follows the analysis presented by Kantorovich *et al.* [38,39]. We identify different signals for the amplitude-modulation (AM) and frequency-modulation (FM) modes within this KPFM model and numerically calculate distance-dependent KPFM maps for the different modes. For these simulations, the capacitive model presented by Sadeghi *et al.* [40] is used for describing the void tip-sample capacitor.

We qualitatively compare the newly derived KPFM model to distance-dependent two-dimensional (2D) KPFM data acquired on a bulk-insulator supported molecular system, namely 2,5-dihydroxybenzoic acid (2,5-DHBA) molecules on calcite (10.4) [18]. It has been identified before that the molecules partly undergo deprotonation, allowing us to study the case of adsorbed dipoles and ionized species [18]. Based on the theoretical analysis, we find that different contributions to the KPFM signal ΔV can be separated by a subtraction of the calcite background data, ultimately allowing us to isolate the KPFM signal originating from the molecular layer.

II. METHODS

Sample preparation and noncontact atomic force microscopy (NC-AFM) experiments were carried out under ultra-high vacuum conditions (base pressure below 1×10^{-10} mbar) at room temperature. Calcite crystals of optical quality were purchased from Korth GmbH [Altenholz (Kiel), Germany] and mechanically cut to the sample holder size [45]. After bringing the samples into vacuum, the crystals were degassed, cleaved, and annealed *in situ*. The annealing step after cleavage is necessary to reduce the quantity of residual charges in the sample [28]. Samples prepared using this strategy result in atomically clean surfaces [46]. The 2,5-dihydroxybenzoic acid molecules were purchased from Sigma-Aldrich (Munich, Germany) with a specified purity of >99%. The molecules were thoroughly outgassed prior to use and deposited *in situ* from a home-built Knudsen cell onto freshly cleaved calcite surfaces

*Present address: Department of Physics and Astronomy, The University of Nottingham, University Park, Nottingham NG7 2RD, United Kingdom; philipp.rahe@nottingham.ac.uk

using a crucible temperature of about 342 K. NC-AFM and FM-KPFM experiments were conducted using an Omicron VT AFM 25 (Omicron Nanotechnology, Taunusstein, Germany) operated in the frequency-modulated [47] mode in beam-deflection configuration. The frequency shift Δf was demodulated using an easyPLL detector (Nanosurf AG, Liestal, Switzerland). For KPFM measurements, an HF2LI device (Zurich Instruments, Zurich, Switzerland) was employed for lock-in detection and feedback loop regulation. We used a FM-KPFM modulation frequency of 987 Hz and a modulation amplitude (zero-peak) of 2 V. All voltages were applied to the tip, while the sample back contact was held at ground. The KPFM signal ΔV is equal to the output of the KPFM feedback loop minimizing the signal amplitude at f_{mod}. It is applied to the tip. Thermal drift along the z direction was monitored and corrected by a home-built atom tracking system [48]. Lateral drift was estimated from the shift in the images acquired before and after each slice data measurement. For the presented data, the residual lateral and vertical drift is smaller than 40 pm/curve, which corresponds to a shift of less than 1 pixel lateral and 3 pixels vertical in the X-Z data. The drift was taken into account when aligning the slice data with the island edges. We used n-doped silicon cantilevers (type PPP-NCH) from NanoWorld (Neuchatel, Switzerland) as probes. Prior to use, the cantilevers were sputtered with Ar^+ at 2 keV for 5 min to remove the oxide layer and surface contaminants.

Numerical calculations are performed in two steps. First, the CAPSOL code presented by Sadeghi *et al.* [40] is employed for calculating the capacitance $C^{(0)}$ and electrostatic potential $\Phi^{(0)}$ of the void tip-sample capacitor. The probe and sample dimensions were chosen close to the experimental conditions and data were calculated over tip-sample distances ranging from typically $d = 0.1$ to $d = 10$ nm with a step size of $\Delta d = 0.01$ nm. The number of grid points suggested by the CAPSOL code was chosen as the minimum number for the calculation. The capacitance and electrostatic potential for exemplary tip-sample distances are presented in Fig. 1 in form of (a) the full two-dimensional distribution of $\Phi^{(0)}$, (b) line profiles along z at $x = 0$ for selected tip-sample distances d, and (c) tip-sample distance-dependent electrostatic potential $\Phi^{(0)}$ at $(x,z) = (0,0.2\ \mathrm{nm})$ (for $U_B = 1$ V) and capacitance $C^{(0)}$.

Second, these data are processed in a MATLAB code to calculate the KPFM signal ΔV for the different KPFM modes. The derivatives needed in the KPFM equations are calculated using finite differences between two immediate neighbors. The integration is performed numerically and poles of the improper integrals are handled by splitting the integral and analytically determining the pole values separately (general AM-KPFM case) or by integration by parts and using higher-order gradients for $\Phi^{(0)}$ and $C^{(0)}$ (general FM-KPFM case), respectively. Point charges $\{q_i\}$ are distributed within the tip-sample capacitor at positions $\{\vec{r}_i\}$. Values of the electrostatic potential $\tilde{\Phi}^{(0)}$ at the point-charge positions $\{\vec{r}_i\}$ are extracted

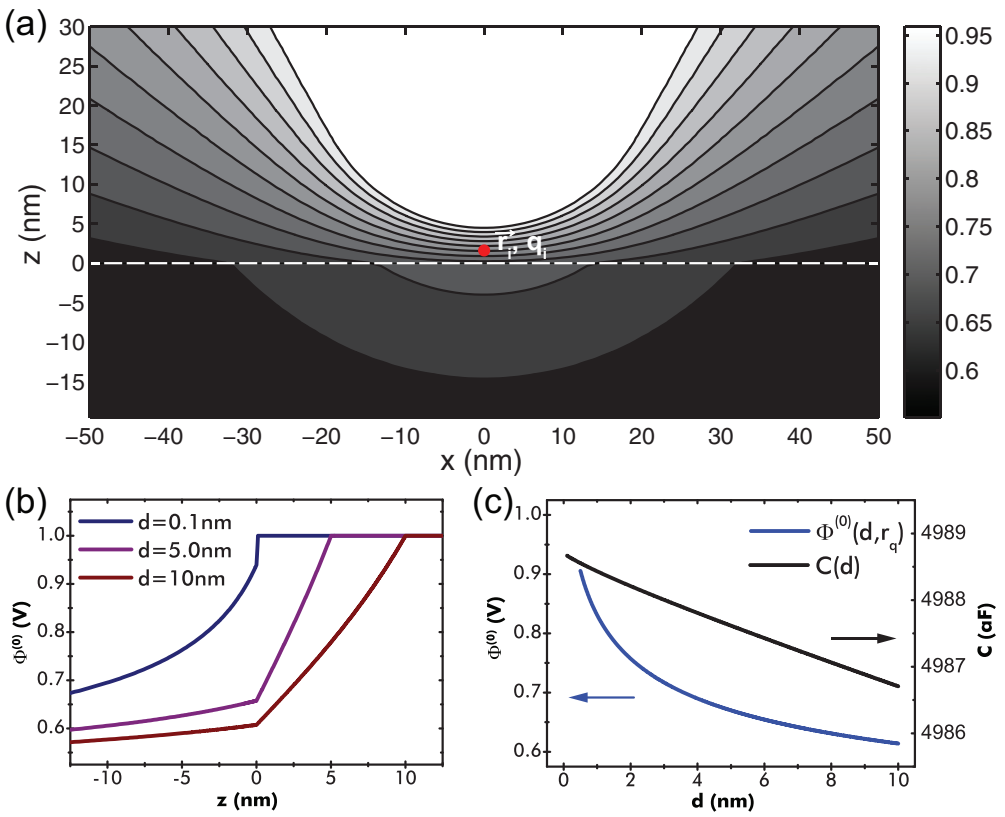

FIG. 1. (Color online) (a) Electrostatic potential distribution for a fixed tip-sample distance of $d = 5$ nm. (b) Vertical line profiles of $\Phi^{(0)}$ at $x = 0$ for selected tip-sample distances d. (c) Electrostatic potential $\Phi^{(0)}$ at $(x,z) = (0,0.2\ \mathrm{nm})$ and capacitance $C^{(0)}$, both with respect to the tip-sample distance d.

from a linear interpolation of the CAPSOL grid positions by using the `TriScatteredInterp` function implemented in MATLAB. KPFM slice data are generated by virtually moving the charges relative to the tip in the void tip-sample capacitor. Thus, the charges are effectively fixed relative to the sample. Finally, these data are used in the formulae derived below to calculate the KPFM signals ΔV.

III. THEORY

We discuss herein the case of a dielectric material forming the underlying substrate. This dielectric sample with dielectric constant ϵ and band gap E_ϵ is partly filling the gap of a capacitor formed by the tip and the sample back contact as visualized in Fig. 2(a). The metals forming the two contacts might have different work functions ϕ_1 and ϕ_2, leading to the contact potential difference $\Delta\phi$ typically measured with KPFM on conducting samples [see Fig. 2(b) for the corresponding band diagram]. In addition, local charges q_i possibly originating from molecular or atomic ions as well as from multipole distributions can be present within the dielectric sample (denoted q_i^ϵ) or within the vacuum gap (denoted q_j^g) of this void capacitor. If charges were also present at the tip (denoted q_k^t), they might be separated from the conducting electrode by a dielectric material ϵ'.

The electrostatic problem of this and related systems has been solved on an abstract level by Kantorovich *et al.* [38,39] by calculating the effective electrostatic energy $W_{\rm el}$ involving an ensemble of point charges $\{q_i\}$ at positions $\{\vec{r}_i\}$ inside a capacitor $C^{(0)}$. This energy also includes the contribution from external batteries which keep the potential on the metal surfaces constant. For an AFM-relevant system the total energy has been found to be

$$W_{\rm el} = -\frac{1}{2}C^{(0)}U_{\rm eff}^2 + \sum_i q_i \Phi^{(0)}(\vec{r}_i) + \frac{1}{2}\sum_i q_i \Phi_{\rm im}(\vec{r}_i) + W_{\rm Coulomb}. \quad (1)$$

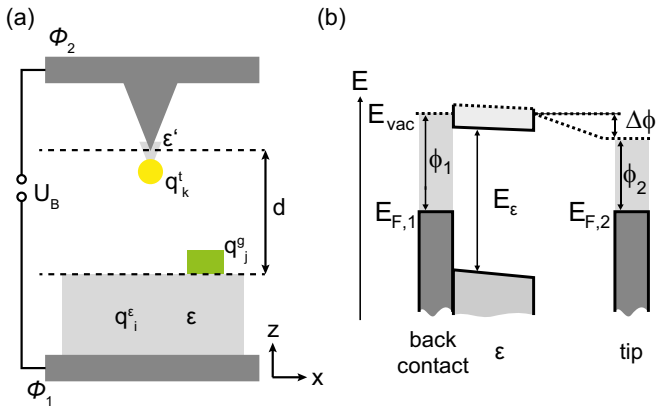

FIG. 2. (Color online) (a) Setup of the tip-sample system considered in the KPFM model, consisting of the void capacitor of tip, dielectric, and sample back contact. Charges (also in the form of dipoles or multipoles) can be present within this void capacitor. (b) Energy diagram of the void tip-sample capacitor, illustrating the contact potential difference $\Delta\phi$ between the sample back contact and the tip.

We introduce the effective potential $U_{\rm eff} = U_B - \frac{\Delta\phi}{e}$ between the metallic plates including a possible difference $\Delta\phi$ of the metallic work functions of tip and sample back contact additionally to the applied voltage U_B. The first term of Eq. (1) describes the energy of the void capacitor with capacitance $C^{(0)}$. This capacitance depends on the tip and sample geometry including the dielectric material, but it is independent of the charge distributions within the capacitor. The second term in Eq. (1) represents the interaction of each point charge q_i with the electrostatic potential $\Phi^{(0)}$ of the void capacitor. The image potential $\Phi_{\rm im}(\vec{r})$ is included in the third term. It can be expressed [39] as $\Phi_{\rm im}(\vec{r}) = \sum_j q_j \Phi_{\rm ind}(\vec{r},\vec{r}_j)$, where $\Phi_{\rm ind}(\vec{r},\vec{r}_j)$ is the electrostatic potential at $\vec{r}$ due to the image charges in the metals caused by a unit point charge at $\vec{r}_j$. The full third term is also known as the image interaction and describes the interaction of each point charge q_i with the image charges of all point charges $\{q_i\}$. The last term describes the pairwise Coulomb interaction between the point charges $\{q_i\}$. Herein, we ignore the contribution due to the reorientation of dipoles in an external electric field. The tip-sample interaction force $F_{\rm el}$ follows directly from

$$F_{\rm el} = -\frac{\partial W_{\rm el}}{\partial d}, \quad (2)$$

where d is defined as the tip-sample distance. Herein, we only include the electrostatic tip-sample interaction. Using Eq. (1), this force can be written as

$$F_{\rm el} = \frac{1}{2}\frac{\partial C^{(0)}}{\partial d}U_{\rm eff}^2 - \sum_i q_i \frac{\partial \Phi^{(0)}(\vec{r}_i)}{\partial d} - \frac{1}{2}\sum_i q_i \frac{\partial \Phi_{\rm im}(\vec{r}_i)}{\partial d} - \frac{\partial}{\partial d}W_{\rm Coulomb}.$$

In this case of two metal bodies, the electrostatic potential of the void capacitor scales linearly with the potential difference between the two metals, $U_{\rm eff} = U_B - \frac{\Delta\phi}{e}$, allowing us to rewrite $\Phi^{(0)} = \tilde{\Phi}^{(0)}U_{\rm eff}$. We then find for the electrostatic tip-sample interaction force $F_{\rm el}$,

$$F_{\rm el} = \frac{1}{2}\frac{\partial C^{(0)}}{\partial d}U_{\rm eff}^2 - \sum_i q_i \frac{\partial \tilde{\Phi}^{(0)}(\vec{r}_i)U_{\rm eff}}{\partial d} - \frac{1}{2}\sum_i q_i \frac{\partial \Phi_{\rm im}(\vec{r}_i)}{\partial d} - \frac{\partial}{\partial d}W_{\rm Coulomb}. \quad (3)$$

Similar formulae have been evaluated for a specific tip-sample system [49,50], while we discuss in the following the general case for different KPFM modes and oscillation amplitudes.

A. AM-KPFM (small oscillation amplitudes A_0)

The AM-KPFM mode measures the direct excitation of the cantilever, usually by applying a modulation voltage at a frequency $f_{\rm mod}$ matching a higher resonance of the cantilever and measuring the amplitude $A_{\rm mod}$ at this frequency [43,51]. For small oscillation amplitudes A_0 of the fundamental mode at f_0, the amplitude $A_{\rm mod}$ is directly proportional to the

electrostatic force F_{el} [52]. This force is minimized with respect to the applied bias U_B to determine the KPFM signal ΔV. Thus, the AM-KPFM condition is generally given by

$$0 = \frac{\partial}{\partial U_B} F_{\mathrm{el}} \quad \left(\text{with } \frac{\partial^2 F_{\mathrm{el}}}{\partial U_B^2} \neq 0\right). \tag{4}$$

We note that this equation is only valid if the oscillation amplitude A_0 of the fundamental cantilever oscillation at f_0 is small; the general case is discussed in the next section. Using Eq. (3), we find for the herein discussed system of point charges $\{q_i\}$ inside a capacitor $C^{(0)}$

$$0 = \frac{\partial C^{(0)}}{\partial d} U_{\mathrm{eff}} - \sum_i q_i \frac{\partial}{\partial U_B}\frac{\partial}{\partial d}\tilde{\Phi}^{(0)}(\vec{r}_i) U_{\mathrm{eff}} - \frac{1}{2}\sum_i q_i \frac{\partial}{\partial U_B}\frac{\partial}{\partial d}\Phi_{\mathrm{im}}(\vec{r}_i) - \frac{\partial}{\partial U_B}\frac{\partial}{\partial d} W_{\mathrm{Coulomb}}. \tag{5}$$

For tip-sample distances d where the tip or sample charges are freely located in the vacuum or dielectric bulk region, but are absent right at the dielectric-vacuum interface and in the metallic tip surface, $\tilde{\Phi}^{(0)}$, Φ_{im}, and W_{Coulomb} including their first derivatives with respect to d and U_B are continuous functions. Thus, Young's theorem allows us to change the order of the derivatives, resulting in the term

$$0 = \frac{\partial C^{(0)}}{\partial d} U_{\mathrm{eff}} - \sum_i q_i \frac{\partial}{\partial d}\frac{\partial}{\partial U_B}\tilde{\Phi}^{(0)}(\vec{r}_i) U_{\mathrm{eff}} - \frac{1}{2}\sum_i q_i \frac{\partial}{\partial d}\frac{\partial}{\partial U_B}\Phi_{\mathrm{im}}(\vec{r}_i) - \frac{\partial}{\partial d}\frac{\partial}{\partial U_B} W_{\mathrm{Coulomb}}. \tag{6}$$

The image potential Φ_{im} does not depend on the applied voltage U_B as it is fully defined by the local charges. Thus, the third term evaluates to zero. Along the same line, the Coulomb interaction W_{Coulomb} between the point charges is also uninfluenced by the applied potential. Thus, the last term also evaluates to zero. By solving for U_B, we find an analytical expression for the AM-KPFM signal, namely

$$\Delta V_{\mathrm{AM-KPFM},1} = U_B = \frac{\Delta\phi}{e} + \frac{\sum_i q_i \frac{\partial}{\partial d}\tilde{\Phi}^{(0)}(\vec{r}_i)}{\frac{\partial C^{(0)}}{\partial d}}. \tag{7}$$

B. AM-KPFM (all oscillation amplitudes A_0)

Usually, the amplitude A_0 of the fundamental oscillation mode at f_0 is larger than the electrically excited amplitude at the first harmonic mode at f_{mod}. In this case, F_{el} is sensed over the oscillation cycle at f_0 where the small amplitude approximation from Sec. III A is unjustified. Based on the detection scheme of NC-AFM operated in a bimodal mode [53,54], an averaging of the electrostatic force over the cantilever oscillation at f_0 is performed where the resulting force has been calculated by integrating along the tip trajectory [40,55]:

$$\overline{F}_{\mathrm{el}} = \frac{1}{\pi}\int_{-A_0}^{A_0} F_{\mathrm{el}}(d + A_0 - \tau)\frac{1}{\sqrt{A_0^2 - \tau^2}}\, d\tau. \tag{8}$$

As before, AM-KPFM minimizes this force with respect to the applied voltage U_B, resulting in the formal condition

$$0 = \frac{\partial}{\partial U_B}\overline{F}_{\mathrm{el}} \quad \left(\text{with } \frac{\partial^2 \overline{F}_{\mathrm{el}}}{\partial U_B^2} \neq 0\right). \tag{9}$$

Given the integration and differentiation are commutative as are the partial derivatives with respect to U_B and d, similar arguments as in the previous section reveal that the last two terms evaluate to zero. Thus, solving Eq. (9) for U_B results in the KPFM signal $\Delta V_{\mathrm{AM-KPFM}}$ for all amplitudes:

$$\Delta V_{\mathrm{AM-KPFM}} = \frac{\Delta\phi}{e} + \frac{\sum_i q_i \int_{-A_0}^{A_0} \frac{\partial}{\partial d}\tilde{\Phi}^{(0)}(\vec{r}_i)\big|_{d+A_0-\tau} \frac{1}{\sqrt{A_0^2-\tau^2}}\, d\tau}{\int_{-A_0}^{A_0} \frac{\partial C^{(0)}}{\partial d}\big|_{d+A_0-\tau} \frac{1}{\sqrt{A_0^2-\tau^2}}\, d\tau}. \tag{10}$$

C. FM-KPFM (small oscillation amplitudes A_0)

In FM-KPFM, the measure minimized with respect to the applied voltage U_B is the frequency shift Δf of the oscillating cantilever. For small amplitudes, this frequency shift is related to the tip-sample interaction force gradient $k_{\mathrm{el}} = -\frac{\partial F_{\mathrm{el}}}{\partial d}$ by [47,56]

$$\Delta f = \frac{f_0}{2k_0} k_{\mathrm{el}} \tag{11}$$

with the free oscillating cantilever frequency f_0 and the cantilever stiffness k_0. Minimizing this signal with respect to U_B leads to the formal FM-KPFM condition

$$0 = \frac{\partial \Delta f}{\partial U_B} = \frac{f_0}{2k_0}\frac{\partial k_{\mathrm{el}}}{\partial U_B} = -\frac{f_0}{2k_0}\frac{\partial}{\partial U_B}\frac{\partial F_{\mathrm{el}}}{\partial d}. \tag{12}$$

By using Eq. (3), this condition evaluates to

$$0 = \frac{\partial^2 C^{(0)}}{\partial d^2} U_{\mathrm{eff}} - \sum_i q_i \frac{\partial}{\partial U_B}\frac{\partial^2}{\partial d^2}\tilde{\Phi}^{(0)}(\vec{r}_i) U_{\mathrm{eff}} - \frac{1}{2}\sum_i q_i \frac{\partial}{\partial U_B}\frac{\partial^2}{\partial d^2}\Phi_{\mathrm{im}}(\vec{r}_i) - \frac{\partial}{\partial U_B}\frac{\partial^2}{\partial d^2} W_{\mathrm{Coulomb}}. \tag{13}$$

Given the continuity of the second derivatives with respect to the tip-sample distance d allows again to eliminate the third and fourth terms due to the missing U_B dependence. Finally, we find the FM-KPFM voltage for small oscillation amplitudes:

$$\Delta V_{\mathrm{FM-KPFM},1} = \frac{\Delta\phi}{e} + \frac{\sum_i q_i \frac{\partial^2}{\partial d^2}\tilde{\Phi}^{(0)}(\vec{r}_i)}{\frac{\partial^2 C^{(0)}}{\partial d^2}}. \tag{14}$$

D. FM-KPFM (all oscillation amplitudes A_0)

For oscillation amplitudes A_0 large compared to the interaction decay length, the frequency shift signal Δf follows from a convolution of the interaction force F_{el} or force gradient k_{el} with weighting functions modeling the cantilever oscillation [56]:

$$\Delta f(d) = \frac{f_0}{\pi k_0 A_0^2}\int_{-A_0}^{A_0} F_{\mathrm{el}}(d + A_0 - \tau)\frac{\tau}{\sqrt{A_0^2 - \tau^2}}\, d\tau \tag{15}$$

$$= -\frac{f_0}{\pi k_0 A_0^2}\int_{-A_0}^{A_0} k_{\mathrm{el}}(d + A_0 - \tau)\sqrt{A_0^2 - \tau^2}\, d\tau. \tag{16}$$

Again, the KPFM technique requires $\frac{\partial \Delta f}{\partial U_B} = 0$, leading to the formal KPFM condition using the electrostatic interaction force and Eq. (15):

$$0 = \frac{f_0}{\pi k_0 A_0^2} \frac{\partial}{\partial U_B} \int_{-A_0}^{A_0} \left[\frac{1}{2} \frac{\partial C^{(0)}}{\partial d}\bigg|_{d+A_0-\tau} U_{\text{eff}}^2 - \sum_i q_i \frac{\partial \tilde{\Phi}^{(0)}(\vec{r}_i) U_{\text{eff}}}{\partial d}\bigg|_{d+A_0-\tau} - \frac{1}{2} \sum_i q_i \frac{\partial \Phi_{\text{im}}(\vec{r}_i)}{\partial d}\bigg|_{d+A_0-\tau} - \frac{\partial W_{\text{Coulomb}}}{\partial d}\bigg|_{d+A_0-\tau} \right] \frac{\tau}{\sqrt{A_0^2 - \tau^2}} d\tau. \quad (17)$$

Given the integration and differentiation are commutative as are the partial derivatives with respect to U_B and d, similar arguments as in the previous sections (charges absent at the vacuum-dielectric, vacuum-tip boundary and inside the tip) reveal that the third and fourth terms evaluate to zero. Solving Eq. (17) for U_B leads to the general FM-KPFM condition

$$\Delta V_{\text{FM-KPFM}} = \frac{\Delta\phi}{e} + \frac{\sum_i q_i \int_{-A_0}^{A_0} \frac{\partial \tilde{\Phi}^{(0)}(\vec{r}_i)}{\partial d}\big|_{d+A_0-\tau} \frac{\tau}{\sqrt{A_0^2-\tau^2}} d\tau}{\int_{-A_0}^{A_0} \frac{\partial C^{(0)}}{\partial d}\big|_{d+A_0-\tau} \frac{\tau}{\sqrt{A_0^2-\tau^2}} d\tau}. \quad (18)$$

E. Theoretical review

The KPFM model described by Eqs. (7), (10), (14), and (18) was derived using several assumptions, both following from or added to the original theory [38,39]. All assumptions, however, are reasonable for the following analysis and experiments.

We reduced the general case of N metals to two metallic surfaces, one representing the tip and the other the sample back contact. Both metals are assumed to be homogeneous in their work function and all charge is assumed to be located at their surfaces. Furthermore, the derivation of Eq. (1) excludes infinite metal surfaces; the tip and sample back contact have to be finite in their geometry [38,39]. All atoms within the tip-sample system are fixed at their respective positions for each tip-sample distance; i.e., relaxations are not considered herein. Thereby, atomic scale contrast formation due to relaxation [31] is not firsthand included.

Equations (7), (10), (14), and (18) allow for a detailed physical understanding of the resulting ΔV signal. First, a homogeneous macroscopic work function difference causes a constant offset to the full KPFM signal as is directly evident from the equations. This difference does not lead to a distance-dependent behavior. Second, the KPFM signal ΔV can be interpreted as the signal arising from charges $\{q_i\}$ probing the potential gradients of $\Phi^{(0)}$ of the void capacitor with respect to d. This fact is evident in the equations as the potential is only evaluated at the positions $\{\vec{r}_i\}$ of the point charges. Consequently, the differences in the potential gradients at the charge positions define the signal in all KPFM modes and especially lead to a spatial "broadening" of the imaged features. The spatial distribution of this KPFM signal can be related to *tip averaging* known from earlier KPFM experiments [49,50,57]. Furthermore, a distance dependency of the KPFM signals is expected as the gradients of $\tilde{\Phi}^{(0)}$ and $C^{(0)}$ are a function of the tip-sample distance d. In turn, $\tilde{\Phi}^{(0)}$ and $C^{(0)}$ are given by the tip-sample geometry as is consequently the KPFM signal on an absolute voltage scale. Third, the KPFM signal is linear in the magnitude of the charges and the signal magnitude is scaled with a possibly weighted average gradient of the tip-sample capacitance $C^{(0)}$. The latter quantity is also tip-sample distance dependent. Last, we note that ΔV shows an additive behavior with respect to the single charge components. This finding suggests a difference scheme to extract single components from the experimental KPFM ΔV data as is introduced later in the context of experimental data.

F. Numerical evaluation

The calculation of the KPFM signal ΔV interestingly only requires us to solve the electrostatic problem of the void capacitor in the absence of the point charges instead of determining the electrostatic potential for the combined charged system. We use the numerical CAPSOL model describing the void tip-sample capacitor as introduced by Sadeghi *et al.* [40] to exemplarily evaluate the KPFM equations. The CAPSOL model is expected to represent our experimental situation more closely than analytical models with simpler geometries [58–60]. The CAPSOL model contains the description of a metallic cantilever, herein evaluated for a half sphere with radius $R_{\text{tip}} = 20$ nm, a tip cone of height $h_{\text{cone}} = 12.5$ μm with a half-opening angle of $\Theta = 25^\circ$ and a disk of radius $R_{\text{cl}} = 34.5$ μm and thickness $t_{\text{cl}} = 4$ μm to simulate the cantilever tip and beam. All dimensions are chosen according to the specification of the probes used in our experiments. The sample is modeled as a dielectric with $\epsilon = 8$ and of thickness $t_{\text{calcite}} = 1$ mm. These values are chosen close to the bulk properties of calcite [61] and the experimental sample geometry [45]. In all calculations, we neglect the constant offset by setting the contact potential difference $\Delta\phi = 0$.

We use Eqs. (7), (10), (14) and (18) to exemplarily calculate the KPFM signal ΔV with the results presented in Fig. 3. The corresponding data for $\Phi^{(0)}$ and $C^{(0)}$ are shown in Fig. 1. The KPFM signal is calculated for a single negative charge located 2Å above the dielectric boundary and for all four measurement conditions, namely amplitude modulation for small A_0 [Fig. 3(a)], amplitude modulation for $A_0 = 2$ nm [Fig. 3(b)], frequency modulation for small A_0 [Fig. 3(c)], and frequency modulation for $A_0 = 2$ nm [Fig. 3(d)].

In all modes, the point charge is clearly revealed in the center of the KPFM slice. However, the magnitude and width of the imaged feature depends on the used KPFM operating conditions as is visible from horizontal line profiles in Fig. 3(f). For KPFM on conducting samples, it has been found before that larger tips generate spatially larger features [49,50,57] and that the FM mode yields improved spatial resolution compared to the AM mode [43,44]. Our simulations reveal a broadening in imaging a point charge and the imaged width appears in this example narrower in the FM compared to the AM-KPFM mode [see normalized line profiles in Fig. 3(f)]. Furthermore, the KPFM signal is observed to be strongly dependent on the tip-sample distance d; see line profiles in Fig. 3(e). The point charge is imaged as a convex feature with nearly constant signals beside the charge position. At the closest tip-sample distances, we find KPFM signals of several hundred millivolts.

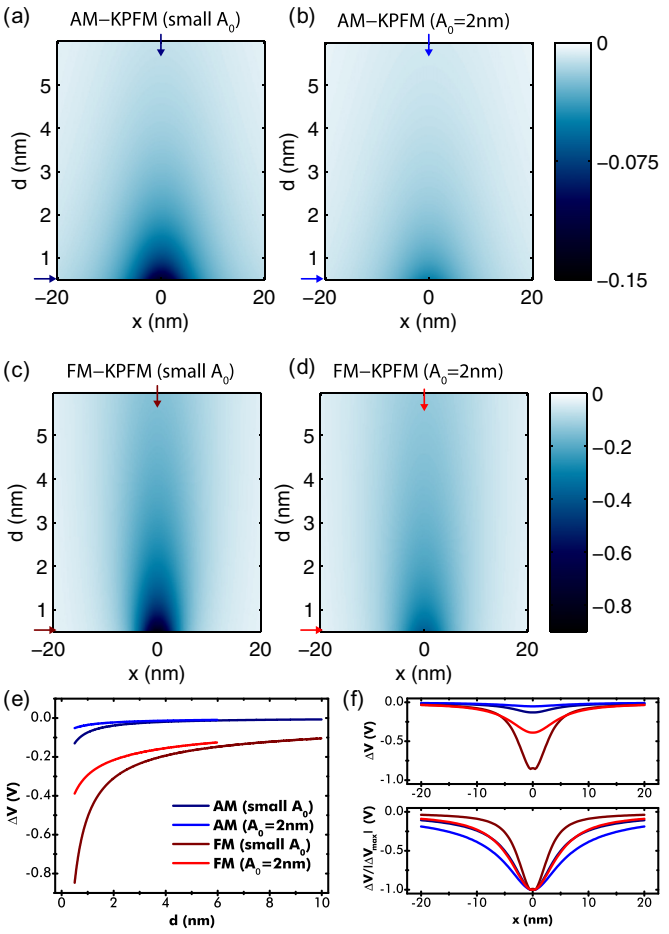

FIG. 3. (Color online) KPFM signal for all four KPFM conditions, namely (a) AM-KPFM for small A_0, (b) AM-KPFM for $A_0 = 2$ nm, (c) FM-KPFM for small A_0, and (d) FM-KPFM for $A_0 = 2$ nm. Data are calculated for a single point charge 2Å above a dielectric sample of thickness 1 mm with $\epsilon = 8$. The same color scale is chosen for each data pair of the AM and FM modes. (e) Comparison of vertical line profiles extracted at the center of each data slice. (f) Top: Horizontal line profiles extracted at the lowest slice position (5Å above the dielectric-vacuum boundary). Bottom: Profiles normalized to each maximum.

The calculated absolute signal is larger for the FM modes compared to the AM-KPFM variant.

IV. EXPERIMENTS

The 2,5-DHBA molecules form small islands of monolayered height when deposited at room temperature on the calcite (10.4) surface under ultrahigh vacuum conditions [18]. An overview is presented in Fig. 4, where the topography data are shown in Fig. 4(a) and KPFM image data are shown in Fig. 4(b). Directly after deposition, two ordered island phases occur, which have been explained by a transition of the molecules from a protonated to a deprotonated state. The molecules in the striped phase form a bulk-like structure which requires protonated molecules. These islands show a weak, negative KPFM contrast which has been attributed to the presence of molecular dipoles [18]. We denote them by "prot" and a symbol of a dipole. The second island type is more

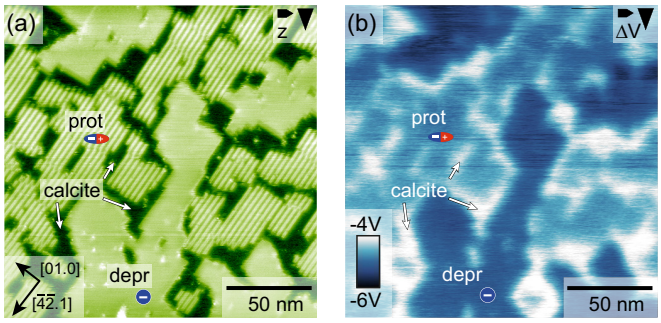

FIG. 4. (Color online) 2,5-DHBA on calcite (10.4). (a) Topography image presenting coexisting protonated (prot, striped appearance) and deprotonated islands (depr) on the calcite substrate (bare calcite surface regions indicated by arrows). (b) Corresponding KPFM image data. Both island types appear darker (more negative) than the bare calcite areas with the deprotonated islands showing the largest negative contrast.

densely packed and exhibits a strong, negative KPFM contrast. The densely packed islands were explained by deprotonated molecules, whose charge results in a strong KPFM signal [18]. We denote them by "depr" and a symbol of a negative charge. Over time, the protonated islands are observed to vanish, while the islands composed of deprotonated molecules grow. Only at high coverage close to one monolayer are both island types stable at room temperature for more than a few hours. All experiments were performed in this and a slightly lower coverage regime, featuring coexisting islands of protonated and deprotonated molecules usually in close proximity.

KPFM slice data

We performed systematic measurements of the KPFM signal ΔV with respect to lateral x and vertical z coordinates, yielding two-dimensional Z-X slices of ΔV data. An automated script was used to reposition the tip along a predefined line on the sample in topography feedback, while a vertical ramp with the deactivated height feedback loop was executed at every lateral position. The data are not corrected for the vertical offset of about 4Å between the calcite surface and the island as this shift is negligible compared to the vertical scale. Thus, the resulting slices represent effectively constant-height data.

Figure 5(a) presents the ΔV signal in a Z-X slice acquired on a sample with a coverage of 2,5-DHBA close to one monolayer (see Appendix for all other measurement channels). At this coverage, the two island phases remain in their respective state over the measurement time span of several hours. A line in the topography data shown in Fig. 5(b) marks the position at which the slice was recorded. The scan was paused a few lines below this position as marked by a small arrow. A shift of about 10 nm along the negative x direction across this line is caused by lateral drift during data acquisition. This drift was considered when assigning the substrate features to the Z-X data as is depicted below the data in Fig. 5(a): From left to right, the KPFM data ΔV maps a protonated island, a narrow gap, a deprotonated island, and again a protonated island.

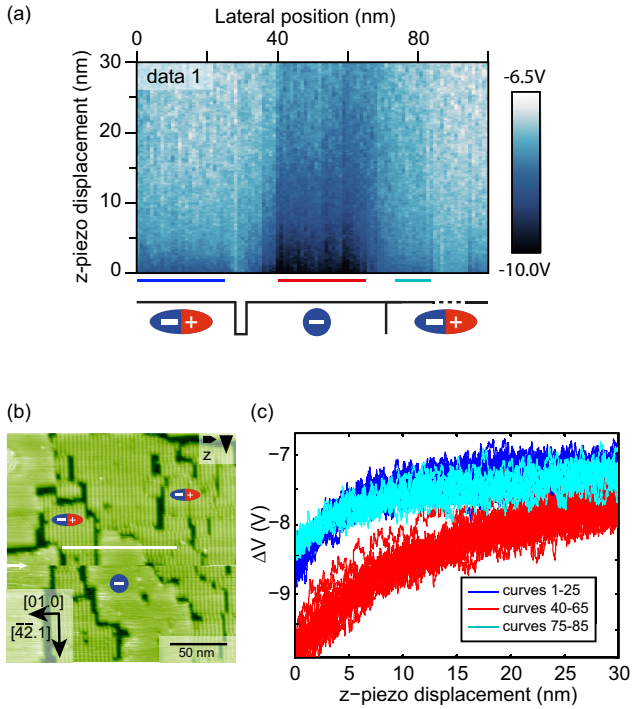

FIG. 5. (Color online) (a) Z-X KPFM data slice on islands of protonated and deprotonated 2,5-DHBA on calcite (10.4). (b) Topography data indicating the position of the slice data, and (c) curves extracted from the protonated (dark and light blue) and deprotonated (red) regimes as marked in (a).

The z-dependent data from several positions at the center of each region are reproduced in Fig. 5(c). Both types of 2,5-DHBA islands on calcite exhibit long-range $\Delta V(z)$ contrast, which extends up to a surprisingly large distance of at least 30 nm in z. Furthermore, the distance behavior differs significantly for the differently charged 2,5-DHBA islands.

Before further discussing the KPFM distance dependence, we perform an identical experiment on a pristine calcite (10.4) surface to investigate the background signal generated by the tip-calcite system itself. Corresponding data are reproduced in Fig. 6, where a distance-dependent ΔV signal is revealed.

Small lateral variations within the lateral width of 100 nm are observed in these data. Although part of the variation lies within the KPFM detection noise level, we explain

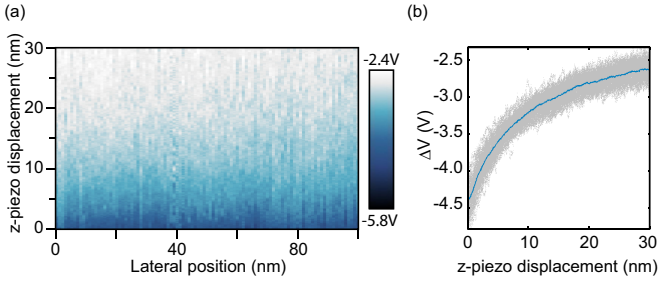

FIG. 6. (Color online) Z-X KPFM data acquired on a pristine calcite (10.4) surface. (a) Slice data showing small lateral variations. (b) Representation of all distance-dependent curves (in gray) and the averaged curve (in blue).

possible lateral variations by charged defects or small polar adsorbates, which are typically present on an *in situ* cleaved ionic crystal [28].

On a pristine, stoichiometric, and nonpolar dielectric material and in the absence of charges inside the capacitor, no distance dependence of the KPFM signal is expected. In this hypothetical case, the KPFM signal is determined solely by the contact potential difference of the homogeneous tip and back contact material [see Eqs. (7), (10), (14), and (18)]. Thus, the observed distance dependence in our experiment points to the presence of additional charges in the tip-sample system. These can be charges in the bulk or at the surface as commonly present after cleavage [28] or being involved in the formation of a surface double layer [62] or other surface relaxations or reconstructions. Furthermore, charges present at the tip apex or shank are also plausible. The presence of localized states with trapped charges has been observed for nominally metallic tips [63] and is also a likely mechanism for silicon probes. Additionally, a distance dependence of the KPFM signal has been interpreted before in terms of the tip state [64]. On a sample with 2,5-DHBA molecules, it is furthermore plausible to assume that molecules were picked up by the tip during scanning, leading to either a dipole or a molecular ion at the tip apex. From a theoretical perspective, however, these charges can be treated similarly to charges on the sample as is evident from Eqs. (7), (10), (14), and (18) with the only difference being that they move when moving the tip. This fact allows for subtracting this background from the molecular KPFM data as introduced in the next section.

V. DISCUSSION

Based on the experimental conditions in KPFM experiments we can further specify the general description of $\{q_i\}$ point charges inside the void capacitor by introducing four possibilities where (partial) charges are present within this system; see also Fig. 7. We assume charges are located at the tip ($Q_{\mathrm{tip},i}$), in the dielectric bulk ($Q_{\mathrm{bulk},i}$), or within the molecular film ($Q_{\mathrm{mol},i}$). Additionally, the molecules or the molecule-surface

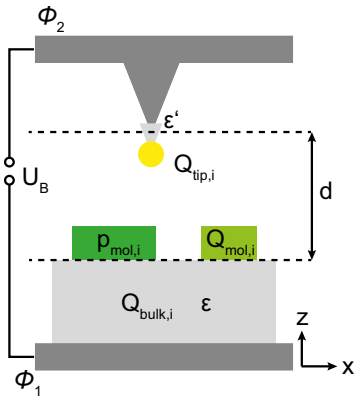

FIG. 7. (Color online) Charges (also in the form of dipoles or multipoles) are abstracted to four regimes within the void capacitor: charges $Q_{\mathrm{tip},i}$ at the tip, $Q_{\mathrm{mol},i}$ in adsorbed molecules, and $Q_{\mathrm{bulk},i}$ in the dielectric substrate as well as dipoles $p_{\mathrm{mol},i}$ of the adsorbed molecular layer.

interface can bear dipoles ($\vec{p}_{\mathrm{mol},i}$). Equations (7), (10), (14), and (18) reveal an additive behavior for each charge to the resulting KPFM signal ΔV. This finding allows us to sort all charges in the tip-sample capacitor into the aforementioned groups and to define the KPFM signal for each of these groups individually. The total KPFM signal ΔV is given as the sum of these individual contributions.

According to this sorting and the model derived above, the KPFM signal on the bare calcite surface is defined by the contact potential difference (CPD) between the electrodes as well as by charges present in the bulk (including charges of parasitic adsorbates after the cleavage process) and at the tip:

$$\Delta V_{\mathrm{calcite}} = \Delta V_{\mathrm{CPD}} + \Delta V_{\mathrm{Qtip}} + \Delta V_{\mathrm{Qbulk}}. \tag{19}$$

On a molecular layer containing charges, the KPFM signal is accordingly given by

$$\Delta V_{\mathrm{Q,layer}} = \Delta V_{\mathrm{CPD}} + \Delta V_{\mathrm{Qtip}} + \Delta V_{\mathrm{Qbulk}} + \Delta V_{\mathrm{Qmol}}. \tag{20}$$

Here, possible charge shifts at the molecule-dielectric interface due to, e.g., ionic relaxations are considered within $\Delta V_{\mathrm{Q,layer}}$. If the molecules only carry a dipole but are not in a charged state, the KPFM signal is described by

$$\Delta V_{\mathrm{p,layer}} = \Delta V_{\mathrm{CPD}} + \Delta V_{\mathrm{Qtip}} + \Delta V_{\mathrm{Qbulk}} + \Delta V_{\mathrm{pmol}}. \tag{21}$$

Again, interface effects are considered within the quantity $\Delta V_{\mathrm{p,layer}}$. Based on this analysis, the sole contribution from the molecular charges and dipoles can be calculated by a simple subtraction of the measured data on top and beside the molecular islands. In particular, this subtraction removes any background signal originating from the CPD of the metallic back contact as well as tip-adsorbed charges and a homogeneous charge distribution within the bulk crystal:

$$\Delta V_{\mathrm{Qmol}} = \Delta V_{\mathrm{Q,layer}} - \Delta V_{\mathrm{calcite}}, \tag{22}$$

$$\Delta V_{\mathrm{pmol}} = \Delta V_{\mathrm{p,layer}} - \Delta V_{\mathrm{calcite}}. \tag{23}$$

This subtraction is possible under the assumption that the electrostatic potential $\Phi^{(0)}$ at the position of the tip due to bulk charges and the capacitance $C^{(0)}$ remain identical for different lateral tip positions and that the charge state of the tip is similar. Additionally, the reference data acquired beside the islands have to be uninfluenced by the charges or multipoles within the island. The latter condition is usually fulfilled if the reference data are acquired at a sufficiently large lateral distance from the island.

Figure 8 presents further data from the DHBA/calcite system, where the KPFM signal is measured systematically across protonated and deprotonated islands. Both data sets were acquired with the same tip on a sample with slightly

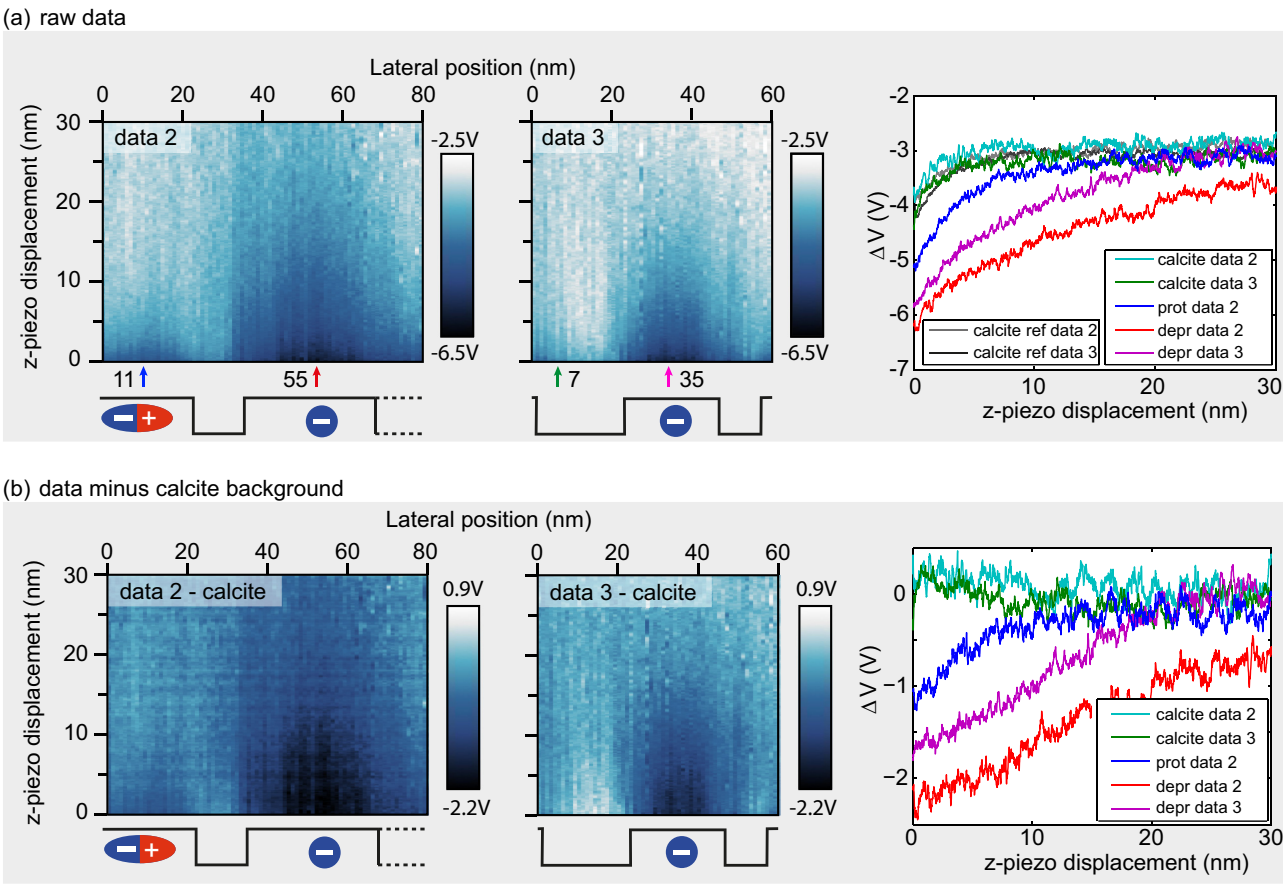

FIG. 8. (Color online) (a) Z-X KPFM data acquired on the molecule-covered calcite (10.4) surface across protonated and deprotonated molecular islands. (b) Data with the calcite background subtracted, following Eqs. (22) and (23). In both panels, lateral slice data across different islands are acquired using the same tip. Vertical line profiles are extracted from these data at the indicated positions and the reference data for subtraction are included in (a), right panel.

lower molecular coverage compared to Fig. 4. In Fig. 8(b), we follow the subtraction strategy justified before. Reference curves acquired on bare calcite areas [see Fig. 8(a), right panel] are subtracted from the raw ΔV data slice in Fig. 8(a). These curves were acquired directly before and after the respective KPFM slice. They were controlled to be identical within the noise limit and averaged to reduce experimental noise. Care was taken to keep sufficient distance from any DHBA islands when acquiring these reference curves, although an upper limit for the separation is given for this specific sample system due to the high molecular coverage. Based on the theory presented above, the resulting difference data then resemble the contribution due to the molecular layer.

Several $\Delta V(z)$ curves extracted from the islands' center positions are reproduced next to the Z-X slices in Fig. 8. In the raw data in Fig. 8(a), most curves converge to a constant value of about -3 V at large tip-sample distances d. This would be in agreement with a constant offset due to the CPD between the sample back contact and the conducting tip according to Eq. (18). Additionally, charges at the tip or in the sample located at positions with potential gradients only barely decaying with the tip-sample distance could lead to an apparent offset within the here-measured height range.

The protonated and deprotonated islands present clearly dissimilar curves. According to the KPFM model, the KPFM signal ΔV is monotonic with the magnitude and number of similar sample charges. Large depr molecular islands are understood to contain more charges than small depr islands as these islands are formed by molecular ions [18]. We observe experimentally an overall larger signal for larger islands as is exemplarily shown in Fig. 8 by the depr curves from data 2 and data 3. This observation is in full agreement with the KPFM model. The signals from depr islands are additionally overall larger than the signal from prot islands. The latter islands are understood to only contain molecular dipoles.

It is furthermore interesting to discuss the distance dependence of the experimental KPFM data. The KPFM model predicts a dependence of ΔV on the tip-sample distance and the numerical example revealed a decreasing signal with a convex shape of charged features in the slice data. The Kelvin signal atop the protonated islands is indeed observed to decay and the island shape is convex. ΔV reaches zero within the noise limit at tip-sample distances larger than about 10 nm for prot islands. The ΔV signal on depr islands is stronger and, thus, converges to zero for d larger than 20 nm.

Precise knowledge of the capacitance and electrostatic potential for this system is required for a quantitative comparison between Eq. (18) and the experimental data. In particular, determining the tip geometry is a challenge in this context. However, we find an excellent qualitative agreement between the experimental data and the theory with the experimental data reproducing characteristic properties of the KPFM model.

VI. CONCLUSIONS

We derived explicit analytical formulae describing the KPFM signal ΔV for a system of point charges in a tip-sample capacitor containing a dielectric sample and for the AM- and FM-KPFM modes. This theoretical model allowed a physical interpretation of the KPFM signal ΔV, revealing that the point charges effectively probe the electrostatic potential gradients of the void tip-sample capacitor. Furthermore, each point charge represents an additive contribution to the total ΔV. From this finding, we suggest a subtraction procedure which allows the extraction of one single-species contribution from the experimentally measured total ΔV.

For a single point charge on a dielectric sample, we exemplarily calculate the KPFM signals ΔV for all modes. We find a large lateral extent of the KPFM signal due to the finite width of the tip and a strong tip-sample distance dependence of ΔV.

The theoretical investigation is supported by experimental distance-dependent 2D FM-KPFM data. The 2,5-DHBA molecules on calcite (10.4) are understood to deliver a system of coexisting molecular dipoles and ions with separated molecular islands formed by protonated or deprotonated molecules, respectively. By subtracting a background signal, which is likely defined by charges in the bulk dielectric or at the tip as well as by the CPD of the back contact and tip, we unravel the plain molecular signal.

In conclusion, this study supplies a detailed understanding of the KPFM signal in charged molecule-insulator systems, including a principle to extract the molecular component, and is expected to help in understanding the complex KPFM contrast formation in future studies.

ACKNOWLEDGMENTS

The support and resources from the Center for High-Performance Computing at the University of Utah are gratefully acknowledged. P.R. is grateful to the Alexander von Humboldt-Foundation for financial support. Experimental results where obtained using the experimental setup in the molecular self-assembly group (Mainz, Germany). J.N. is grateful to Markus Kittelmann for sharing his knowledge about the coverage-dependent kinetics of 2,5-DHBA on calcite and to Stefan Kuhn for experimental support. We furthermore thank Lev Kantorovich, Clayton C. Williams, Ralf Bechstein, and Hagen Söngen for most fruitful discussions and Ali Sadeghi for most helpful support with setting up the CAPSOL calculations.

APPENDIX: ALL MEASUREMENT CHANNELS

During the acquisition of KPFM Z-X data, a total of five measurement channels are recorded: frequency shift (Δf), KPFM error signal (δV), KPFM signal (ΔV), amplitude (A), and dissipation (Γ) (see Fig. 9). Phase-locked loop (PLL), amplitude, and KPFM feedbacks are engaged during acquisition of each curve, while the topography feedback loop is switched off during data acquisition. Each curve was started close to the sample by typically retracting the tip by 30 nm while sampling 2000 points. The retract curve is followed by an approach curve with the same number of data points. An acquisition time between 10 and 20 ms was used at each data point and a total of typically 75–150 lateral positions across a distance of about 50 to 150 nm were chosen. The total time for a full slice was on the order of about 1.5 h. To reduce effects from thermal drift and scanner creep, the drift along

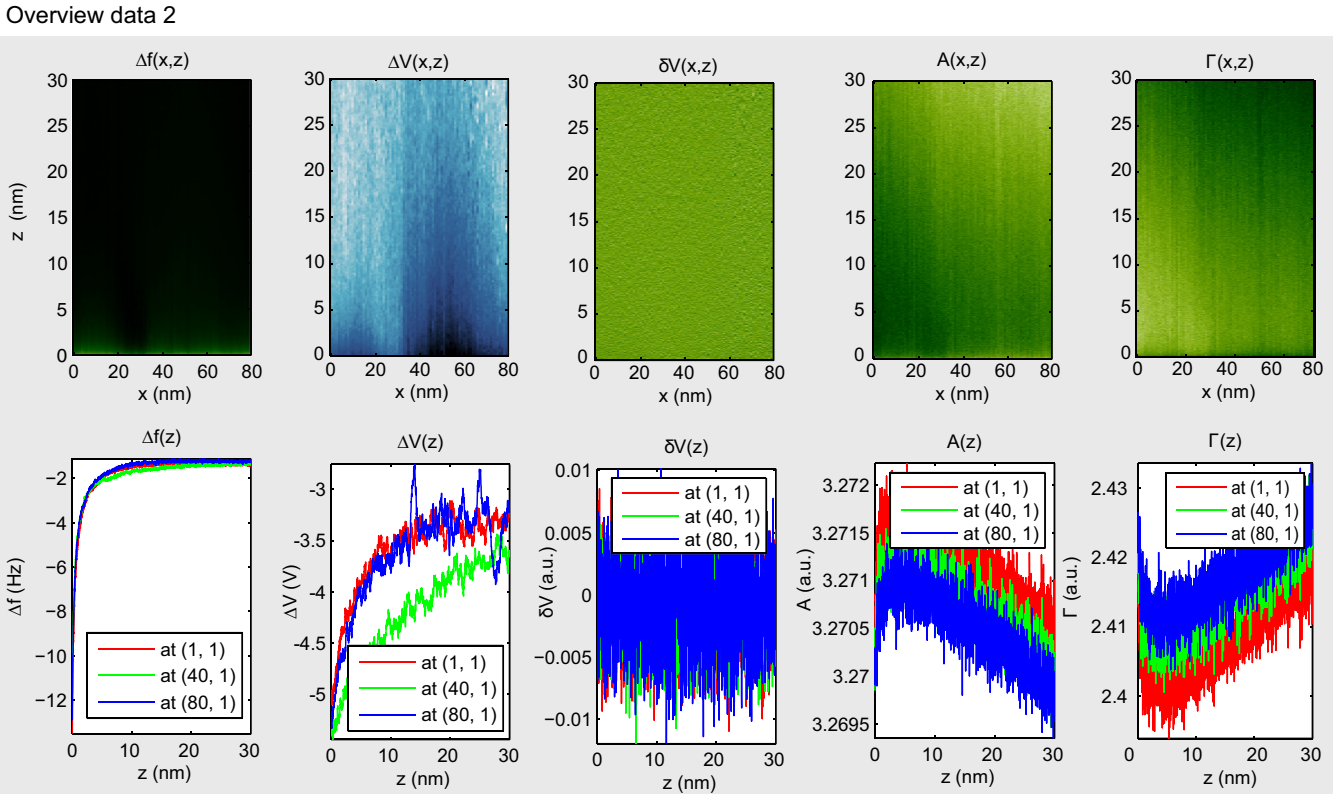

FIG. 9. (Color online) Representation of all measurement channels in a KPFM slice experiment: frequency shift (Δf), KPFM signal (ΔV), KPFM error signal (δV), amplitude (A), and dissipation (Γ) raw data.

z was measured and corrected initially using a home-built atom-tracking system [48]. Additionally, the z feedback is enabled for several seconds between each curve to readjust the z position and to compensate for scanner creep.

Figure 9 shows all recorded channels of the Z-X data shown in Fig. 8 (data 2). The top row presents the data as slices, and the lower row depicts three selected curves, namely the first (at $x = 0$ nm), the middle (at $x = 40$ nm), and the last (at $x = 80$ nm). The error signal for the KPFM feedback loop reveals only noise, identifying a properly working feedback loop. Furthermore, the amplitude feedback was also working correctly beside the narrow z range [0 nm, 3 nm] close to the sample. The decrease in amplitude and increase in dissipation along z is attributed to an artifact of the measurement system. Variations of amplitude and dissipation with different absolute z-piezo positions are frequently observed with the used microscope. This effect is tentatively explained by a nonlinear transfer function between the excitation signal amplitude for the excitation piezo and the resulting cantilever oscillation amplitude [65]. As no similar variations are observed in the other channels, crosstalk is unlikely. Moreover, these variations are below 0.1%.

[1] G. Binnig, C. F. Quate, and Ch. Gerber, Phys. Rev. Lett. **56**, 930 (1986).
[2] L. Kelvin, Philos. Mag. Ser. 5 **46**, 82 (1898).
[3] M. Nonnenmacher, M. P. O'Boyle, and H. K. Wickramasinghe, Appl. Phys. Lett. **58**, 2921 (1991).
[4] W. Melitz, J. Shen, A. C. Kummel, and S. Lee, Surf. Sci. Rep. **66**, 1 (2011).
[5] C. Barth, A. S. Foster, C. R. Henry, and A. L. Shluger, Adv. Mater. **23**, 477 (2011).
[6] *Kelvin Probe Force Microscopy*, edited by S. Sadewasser and T. Glatzel, Springer Series in Surface Sciences (Springer, Heidelberg, 2012).
[7] T. Glatzel, D. F. Marron, T. Schedel-Niedrig, S. Sadewasser, and M. C. Lux-Steiner, Appl. Phys. Lett. **81**, 2017 (2002).
[8] S. Sadewasser, T. Glatzel, M. Rusu, A. Jager-Waldau, and M. C. Lux-Steiner, Appl. Phys. Lett. **80**, 2979 (2002).
[9] S. Sadewasser, T. Glatzel, S. Schuler, S. Nishiwaki, R. Kaigawa, and M. C. Lux-Steiner, Thin Solid Films **431**, 257 (2003).
[10] C. Barth and C. R. Henry, Appl. Phys. Lett. **89**, 252119 (2006).
[11] C. Barth and C. R. Henry, J. Phys. Chem. C **113**, 247 (2009).
[12] D. Stöffler, S. Fostner, P. Grütter, and R. Hoffmann-Vogel, Phys. Rev. B **85**, 033404 (2012).
[13] J. Lü, L. Eng, R. Bennewitz, E. Meyer, H.-J. Güntherodt, E. Delamarche, and L. Scandella, Surf. Interface Anal. **27**, 368 (1999).
[14] V. Palermo, M. Palma, and P. Samorì, Adv. Mater. **18**, 145 (2006).
[15] U. Zerweck, C. Loppacher, T. Otto, S. Grafström, and L. M. Eng, Nanotechnology **18**, 084006 (2007).
[16] A. Liscio, V. Palermo, D. Gentilini, F. Nolde, K. Müllen, and P. Samorí, Adv. Funct. Mater. **16**, 1407 (2006).

[17] S. A. Burke, J. M. LeDue, Y. Miyahara, J. M. Topple, S. Fostner, and P. Grutter, Nanotechnology **20**, 264012 (2009).

[18] M. Kittelmann, P. Rahe, A. Gourdon, and A. Kühnle, ACS Nano **6**, 7406 (2012).

[19] S. Kawai, A. Sadeghi, X. Feng, P. Lifen, R. Pawlak, T. Glatzel, A. Willand, A. Orita, J. Otera, S. Goedecker, and E. Meyer, ACS Nano **7**, 9098 (2013).

[20] L. Gross, F. Mohn, P. Liljeroth, J. Repp, F. J. Giessibl, and G. Meyer, Science **324**, 1428 (2009).

[21] L. Nony, A. S. Foster, F. Bocquet, and C. Loppacher, Phys. Rev. Lett. **103**, 036802 (2009).

[22] F. Mohn, L. Gross, N. Moll, and G. Meyer, Nat. Nanotechnol. **7**, 227 (2012).

[23] N. Moll, B. Schuler, S. Kawai, F. Xu, L. Peng, A. Orita, J. Otera, A. Curioni, M. Neu, J. Repp, G. Meyer, and L. Gross, Nano Lett. **14**, 6127 (2014).

[24] B. Schuler, A.-X. Liu, Y. Geng, S. Decurtis, G. Meyer, and L. Gross, Nano Lett. **14**, 3342 (2014).

[25] T. Leoni, O. Guillermet, H. Walch, V. Langlais, A. Scheuermann, J. Bonvoisin, and S. Gauthier, Phys. Rev. Lett. **106**, 216103 (2011).

[26] P. Rahe, R. P. Steele, and C. C. Williams (unpublished).

[27] H. H. Pieper, C. Barth, and M. Reichling, Appl. Phys. Lett. **101**, 051601 (2012).

[28] C. Barth and C. R. Henry, Nanotechnology **17**, 155 (2006).

[29] L. Gross, B. Schuler, F. Mohn, N. Moll, N. Pavliček, W. Steurer, I. Scivetti, K. Kotsis, M. Persson, and G. Meyer, Phys. Rev. B **90**, 155455 (2014).

[30] F. Bocquet, L. Nony, C. Loppacher, and T. Glatzel, Phys. Rev. B **78**, 035410 (2008).

[31] F. Bocquet, L. Nony, and C. Loppacher, Phys. Rev. B **83**, 035411 (2011).

[32] T. Glatzel, L. Zimmerli, S. Koch, S. Kawai, and E. Meyer, Appl. Phys. Lett. **94**, 063303 (2009).

[33] E. J. Spadafora, M. Linares, Nisa Yahya, Wan Zaireen, F. Lincker, R. Demadrille, and B. Grevin, Appl. Phys. Lett. **99**, 233102 (2011).

[34] A. Hinaut, A. Pujol, F. Chaumeton, D. Martrou, A. Gourdon, and S. Gauthier, Beilstein J. Nanotechnol. **3**, 221 (2012).

[35] J. L. Neff, P. Milde, C. Prez Len, M. D. Kundrat, L. M. Eng, C. R. Jacob, and R. Hoffmann-Vogel, ACS Nano **8**, 3294 (2014).

[36] B. Hoff, M. Gingras, R. Peresutti, C. R. Henry, A. S. Foster, and C. Barth, J. Phys. Chem. C **118**, 14569 (2014).

[37] S. Hudlet, M. Saint Jean, B. Roulet, J. Berger, and C. Guthmann, J. Appl. Phys. **77**, 3308 (1995).

[38] L. N. Kantorovich, A. I. Livshits, and M. Stoneham, J. Phys.: Condens. Matter **12**, 795 (2000).

[39] L. N. Kantorovich, A. S. Foster, A. L. Shluger, and A. M. Stoneham, Surf. Sci. **445**, 283 (2000).

[40] A. Sadeghi, A. Baratoff, S. A. Ghasemi, S. Goedecker, T. Glatzel, S. Kawai, and E. Meyer, Phys. Rev. B **86**, 075407 (2012).

[41] G. Cohen, E. Halpern, S. U. Nanayakkara, J. M. Luther, C. Held, R. Bennewitz, A. Boag, and Y. Rosenwaks, Nanotechnology **24**, 295702 (2013).

[42] K. Wandelt, Appl. Surf. Sci. **111**, 1 (1997).

[43] T. Glatzel, S. Sadewasser, and M. C. Lux-Steiner, Appl. Surf. Sci. **210**, 84 (2003).

[44] U. Zerweck, C. Loppacher, T. Otto, S. Grafström, and L. Eng, Phys. Rev. B **71**, 125424 (2005).

[45] L. Tröger, J. Schütte, F. Ostendorf, A. Kühnle, and M. Reichling, Rev. Sci. Instrum. **80**, 063703 (2009).

[46] P. Rahe, J. Schütte, and A. Kühnle, J. Phys.: Condens. Matter **24**, 084006 (2012).

[47] T. R. Albrecht, P. Grütter, D. Horne, and D. Rugar, J. Appl. Phys. **69**, 668 (1991).

[48] P. Rahe, J. Schütte, W. Schniederberend, M. Reichling, M. Abe, Y. Sugimoto, and A. Kühnle, Rev. Sci. Instrum. **82**, 063704 (2011).

[49] C. Barth, T. Hynninen, M. Bieletzki, C. R. Henry, A. S. Foster, F. Esch, and U. Heiz, New J. Phys. **12**, 093024 (2010).

[50] T. Hynninen, A. S. Foster, and C. Barth, e-J. Surf. Sci. Nanotechnol. **9**, 6 (2011).

[51] A. Kikukawa, S. Hosaka, and R. Imura, Rev. Sci. Instrum. **67**, 1463 (1996).

[52] Technical aspects of the lock-in-based detection including the information available from the 2ω signal are ignored within this context. Furthermore, we do not discuss consequences of the applied ac voltage.

[53] S. Kawai, T. Glatzel, S. Koch, B. Such, A. Baratoff, and E. Meyer, Phys. Rev. Lett. **103**, 220801 (2009).

[54] S. Kawai, T. Glatzel, S. Koch, B. Such, A. Baratoff, and E. Meyer, Phys. Rev. B **81**, 085420 (2010).

[55] S. Kawai, T. Glatzel, H. J. Hug, and E. Meyer, Nanotechnology **21**, 245704 (2010).

[56] F. J. Giessibl, Phys. Rev. B **56**, 16010 (1997).

[57] T. Glatzel, L. Zimmerli, S. Koch, B. Such, S. Kawai, and E. Meyer, Nanotechnology **20**, 264016 (2009).

[58] A. Sadeghi, A. Baratoff, and S. Goedecker, Phys. Rev. B **88**, 035436 (2013).

[59] T. Sometani, Eur. J. Phys. **21**, 549 (2000).

[60] W. R. Smythe, *Static and Dynamic Electricity* (McGraw-Hill, New York, 1950), Chap. 5.

[61] K. Rao and K. Rao, Z. Phys. A Hadrons Nucl. **216**, 300 (1968).

[62] C. Barth and C. R. Henry, Phys. Rev. Lett. **98**, 136804 (2007).

[63] G. Teobaldi, K. Lämmle, T. Trevethan, M. Watkins, A. Schwarz, R. Wiesendanger, and A. L. Shluger, Phys. Rev. Lett. **106**, 216102 (2011).

[64] C. Sommerhalter, T. Glatzel, T. Matthes, A. Jäger-Waldau, and M. Lux-Steiner, Appl. Surf. Sci. **157**, 263 (2000).

[65] A. Labuda, Y. Miyahara, L. Cockins, and P. H. Grütter, Phys. Rev. B **84**, 125433 (2011).